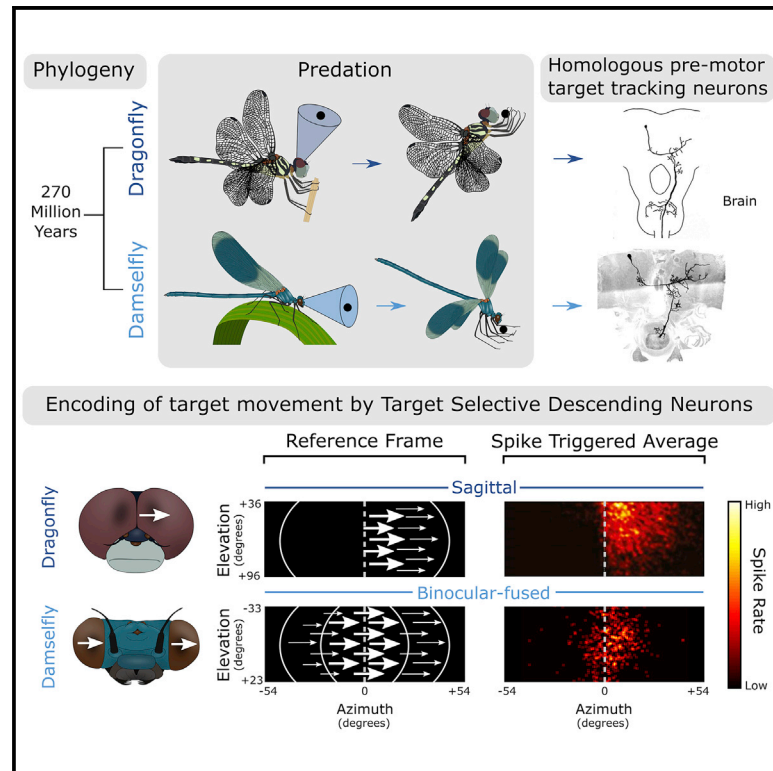# Current Biology

# Binocular Encoding in the Damselfly Pre-motor Target Tracking System

## Graphical Abstract



## Authors

Jack A. Supple, Daniel Pinto-Benito, Christopher Khoo, ..., Hanchuan Peng, Robert M. Olberg, Paloma T. Gonzalez-Bellido

## Correspondence

paloma@umn.edu

## In Brief

Supple et al. link the divergent eye morphology and hunting strategies of dragonflies and damselflies. Target-selective descending neurons in these two groups are identified as homologous, but damselfly TSDNs face forward and encode information in a binocular-fused reference frame.

## Highlights

- Demoiselles align their prey frontally during predatory flights

- Target-selective descending neurons are homologous in dragonflies and damselflies

- TSDN reference frame is binocular-fused in damselflies but sagittal in dragonflies

- Summation to threshold explains binocular responses of demoiselle TSDNs

CellPress

# Article

# Binocular Encoding in the Damselfly Pre-motor Target Tracking System

Jack A. Supple,[1] Daniel Pinto-Benito,[1] Christopher Khoo,[1] Trevor J. Wardill,[1,2] Samuel T. Fabian,[1] Molly Liu,[2] Siddhant Pusdekar,[2] Daniel Galeano,[2] Jintao Pan,[3] Shengdian Jiang,[3] Yimin Wang,[3,4] Lijuan Liu,[3] Hanchuan Peng,[3] Robert M. Olberg,[5] and Paloma T. Gonzalez-Bellido[2,6,*]

[1]Department of Physiology, Development, and Neuroscience, University of Cambridge, Downing Street, Cambridge CB3 2EG, UK
[2]Department of Ecology, Evolution, and Behavior, University of Minnesota, Saint Paul, MN 55108, USA
[3]SEU-Allen Joint Center, Institute for Brain and Intelligence, Southeast University, Nanjing 210096, China
[4]School of Computer Engineering and Science, Shanghai University, Shanghai 200444, China
[5]Department of Biological Sciences, Union College, Schenectady, NY 12308, USA
[6]Lead Contact
*Correspondence: paloma@umn.edu
https://doi.org/10.1016/j.cub.2019.12.031

## SUMMARY

Akin to all damselflies, *Calopteryx* (family *Calopterygidae*), commonly known as jewel wings or demoiselles, possess dichoptic (separated) eyes with overlapping visual fields of view. In contrast, many dragonfly species possess holoptic (dorsally fused) eyes with limited binocular overlap. We have here compared the neuronal correlates of target tracking between damselfly and dragonfly sister lineages and linked these changes in visual overlap to pre-motor neural adaptations. Although dragonflies attack prey dorsally, we show that demoiselles attack prey frontally. We identify demoiselle target-selective descending neurons (TSDNs) with matching frontal visual receptive fields, anatomically and functionally homologous to the dorsally positioned dragonfly TSDNs. By manipulating visual input using eyepatches and prisms, we show that moving target information at the pre-motor level depends on binocular summation in demoiselles. Consequently, demoiselles encode directional information in a binocularly fused frame of reference such that information of a target moving toward the midline in the left eye is fused with information of the target moving away from the midline in the right eye. This contrasts with dragonfly TSDNs, where receptive fields possess a sharp midline boundary, confining responses to a single visual hemifield in a sagittal frame of reference (i.e., relative to the midline). Our results indicate that, although TSDNs are conserved across Odonata, their neural inputs, and thus the upstream organization of the target tracking system, differ significantly and match divergence in eye design and predatory strategies.

## INTRODUCTION

Despite sampling the visual world through two eyes, our brain fuses these images into a cyclopean percept with a single point of view [1]. Binocular image fusion imparts several perceptual advantages, including enhanced visual sensitivity [2, 3], decreased reaction times [4], and the potential to calculate depth from image disparity [5, 6]. As such, binocularity is often found in visually guided predatory species [7].

Odonata is an ancient predatory lineage comprising two distinctive extant sister groups, the damselflies (Zygoptera) and dragonflies (Epiprocta, comprising Anisoptera and Epiophlebioptera; Figure S1A). Damselflies and dragonflies share a last common ancestor ~270 million years ago (mya) and have subsequently diverged in behavior and anatomy [8, 9]. Dragonflies are well known for their large, round compound eyes and agile interception flights to catch flying prey [10]. To date, a large body of work describes the behavioral and neurophysiological mechanisms underlying target interception in dragonflies [10–18]. Such studies have focused on abundant anisopteran dragonflies (families *Aeshnoidea*, *Corduliidae*, and *Libellulidea*) that intercept prey from below, stabilizing the prey image upon a cyclopean dorsal fovea [10–18]. This fovea is formed by fusing the compound eyes at the dorsal surface into a continuous plane of ommatidia with reduced binocular overlap, known as a holoptic eye [19].

Target movement across the dragonfly dorsal fovea (Figure 1Ai) is encoded at the pre-motor level by a small population of eight bilaterally symmetric target-selective descending neurons (TSDNs) [11, 13, 20]. TSDNs receive input from the lateral protocerebrum and project to the subesophageal ganglion (SOG) and thoracic motor centers with a total latency of less than 30 ms [11, 13, 20]. Each TSDN type possesses a characteristic receptive field that is directionally tuned and spatially localized to a specific region of the dorsal visual field [11]. As a population, TSDNs primarily encode target movement away from or along the midline [11], and TSDN firing can change the angle of attack and beating of the wings (R.M. Olberg, 1983, Soc. Neurosci., abstract) [21], presumably reflecting their role as part of a reactive steering mechanism keeping the dragonfly locked onto the prey during pursuit [11].

The holoptic eye morphology of extant dragonflies appears to be a secondarily derived trait, which has evolved repeatedly within the Odonatoptera superorder throughout the last 320 mya [8, 22]. Holoptic eyes are absent in all damselflies, several extant dragonfly lineages (families *Gomphoidea*, *Petaluroidea*,
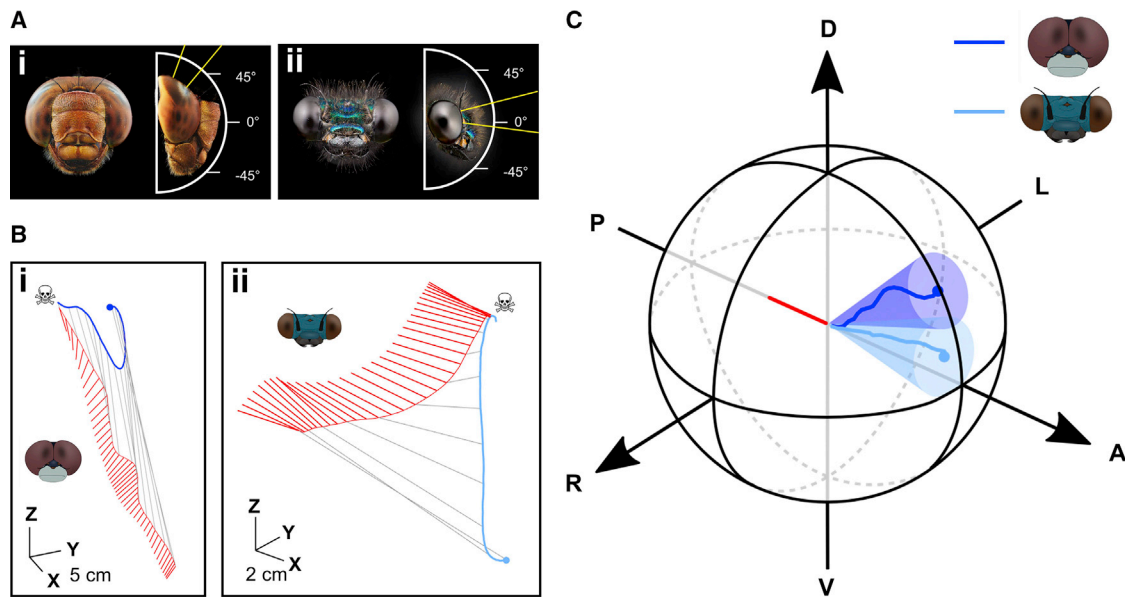
**Figure 1. Comparison of External Eye Anatomy and Hunting Strategies of Dragonflies and Damselflies**

(A) Frontal and lateral views of a dragonfly with holoptic eyes (*Sympetrum vulgatum*) and a demoiselle damselfly with dichoptic eyes (*Calopteryx splendens*). Yellow lines indicate visual area sampled by the dorsal (~60° elevated in dragonflies) [10] and frontal foveae, respectively.

(B) Predatory flights of a dragonfly (i, *Erythemis simplicicollis*; Figure S1B; Video S1) and demoiselle (ii, *Calopteryx aequabilis*; Figure S1C; Video S2) while chasing an artificial prey (blue) reconstructed in 3D. Predator head positions are represented as a continuous red curve, with the body axis plotted at 10-ms intervals to indicate orientation of the predator throughout the attack (red lines). Line of sight between predator head position and artificial prey in gray.

(C) Spherical plots, tracing the average subtended position of the prey (blue) compared to the body axis of the predator throughout the flight (red). Cones depict the 95% confidence interval (CI) of the prey just before the predator's first movement. In dragonfly attacks, the prey (dark blue) was on average aligned above the dragonfly body axis by 32.6° just prior to the first movement of the predator (95% CI = ±12.4°; n = 8) and by 33.7° throughout flight (95% CI = ±5.3°; n = 8). In demoiselle attacks, the prey (light blue) was on average aligned above the body axis by 13.9° just prior to the first movement of the predator (95% CI = ±13.0°; n = 10) and by 11.4° throughout flight (95% CI = ±6.5°; n = 10). A, anterior; D, dorsal; L, left; p, posterior; R, right; V, ventral.

and the basal dragonfly lineage *Epiophlebiidae*; Figure S1A) and extinct archaic odonatopterans [23]. Instead, all damselflies have two conspicuously separated (dichoptic) compound eyes [9, 24]. Hitherto, little is known about the anatomical and neuronal specializations facilitating predation in any damselfly [24]. Although most damselflies are known to hunt by snatching stationary prey from a substrate, a behavior termed gleaning [9, 25], the demoiselle damselflies (*Calopterygidae*) are thought only to attack flying prey [9, 26], somewhat similar to dragonflies. Demoiselles are thus uniquely placed within Zygoptera to investigate how frontal-facing foveae with large interocular distance (Figure 1Aii) may influence prey-tracking circuits, especially in comparison to those described in dragonflies.

In this study, we investigate how the divergences between damselflies and dragonflies at the level of visual anatomy are reflected in their predatory tactic and target-tracking circuitry. In comparison to dragonflies, we found that damselflies attack when their prey is positioned more frontally, rather than dorsally, in the visual field. We also report that this frontal area of the visual field in damselflies is sampled by TSDNs homologous to those of dragonflies. Unlike the holoptic dragonflies studied to date, all TSDN responses in damselflies integrate information from both eyes and they encode target direction in a binocular, fused reference frame. This is distinctly different from holoptic dragonflies, whose TSDNs encode direction of a moving target in a sagittal reference frame relative to the midline formed by their two merged eyes.

## RESULTS

### Demoiselles Attack Prey Head on

As previously reported [10, 12, 15], we found that dragonflies approach their prey from below (Figure 1Bi; Video S1), tracking targets within the dorsal fovea. Just prior to and throughout the flight, the prey aligned above the dragonfly body azimuth on average 32.6° (95% confidence interval, CI = ±12.4°; n = 8) and 33.7° (95% CI = ±5.3°; n = 8), respectively (Figures 1C and S1B; Video S1).

In contrast, we found that damselflies fly to the elevation of the target (Figure 1Bii), keeping it in the frontal aspect of their visual field before lunging forward to grasp it (Video S2). We found that, just prior to and throughout the flight, the prey aligned above the demoiselle body azimuth on average 13.9° (95% CI = ±13.0°; n = 5) and 11.4° (95% CI = ±6.5°; n = 10), respectively (Figures 1C and S1C; Video S2).

Both measures of prey location here reported, i.e., above the body axis prior to the initiation of flight and throughout flight, were statistically significantly different between dragonflies and demoiselles (p = 0.0441 and p = 6.98e−05, respectively; Watson-Williams tests).

### TSDNs Serving the Demoiselle Frontal Fovea

We next investigated how the more frontal predatory behavior and dichoptic ocular arrangement of demoiselles is reflected in their target-tracking system. In multiunit recordings from the

demoiselle ventral nerve cord, responses to small moving objects were confined to the frontal visual field (Figure 2A). Thus, we positioned the animals and visual stimuli accordingly (Figures 2B, S2A, and S2B). We first recorded target responses from the ventral nerve cord with extracellular tungsten electrodes, and after spike sorting (Figure S2C; STAR Methods), we calculated the latency (Figures S3A and S3B), spike-triggered averages, and directional tuning maps (Figure S3C).

We discovered demoiselle descending neurons that shared distinguishing features with dragonfly TSDNs: (1) robust responses to small targets of fixed size that moved in cardinal directions; (2) directional tuning; and (3) no sustained responses to wide-field stimuli (Figure S3C) [11, 13]. We classified these cells as demoiselle TSDNs and assigned them to previously described dragonfly TSDN cell types [11] according to the position and direction tuning of their receptive fields (Figures 2C and S3; we putatively recorded the following number of cells for each TSDN type: MDT1 = 12, MDT2 = 6, MDT3 = 4, MDT4 = 8, MDT5 = 4, DIT1 = 5, DIT2 = 9, and DIT3 = 7). We found that the response properties of demoiselle TSDNs are qualitatively very similar in directional selectivity to those previously described in dragonflies [11], and the overall tuning curves for moving targets appear to be remarkably conserved (Figures 2C and S3C).

We hypothesized that demoiselle TSDNs would not only be functionally similar to dragonfly TSDNs but also anatomically similar. To link anatomy and function, we recorded the responses from the demoiselle TSDNs intracellularly (Figure 2C, rows marked "*") and loaded them with fluorescent dye at the end of the recording. The receptive field location and the directional tuning of these intracellularly identified neurons were consistent with those isolated extracellularly (Figure 2C), validating our extracellularly recorded receptive fields. Our intracellular maps appear sparser due to a reduced mapping stimulus (1.3 versus 20 min), as we aimed to maximize time for dye loading. Lines of activity are observed due to the longer, rasterized target trajectories presented across the visual field with this reduced stimulus. The cell body position and arborization pattern of all demoiselle TSDNs (Videos S3 and S4) matched closely those of dragonflies (Figure 3) [13, 20], with the majority of demoiselle TSDN cell bodies (i.e., DIT1, DIT2, MDT2, MDT4, and MDT5) also arising from the n-ventral cell body cluster ("n-" relative to the neuraxis) [27]. Together, the anatomical and electrophysiological properties of demoiselle TSDNs demonstrate that these neurons are homologous.

Our intracellular dataset further confirms that both the spike rate and overall binocular extent of a single TSDN type can differ substantially across animals (Figure 4). Given these properties, responses to moving targets alone are not sufficient to distinguish with absolute certainty between some TSDNs, even though we always recorded from the right connective in demoiselles. This is the case for all three ipsilateral cells responsive to targets moving toward the right of the animal (MDT2/DIT2/MDT3). The same ambiguity exists between the two contralateral cells responsive to targets moving toward the left (DIT1/DIT3). This ambiguity, however, does not change the conclusions from our findings, in this or the following sections. In addition to the high variability of responses within TSDN types, our recordings point toward the possibility that more

than eight pairs of forward-looking TSDNs exist in demoiselles (see Figure S4).

Although demoiselle and dragonfly TSDNs share many characteristics, we also found important differences, most strikingly in the extent of overlap across the visual midline (Figure 2C). The receptive fields of most dragonfly TSDNs display a sharp vertical boundary at or just over the midline, confining responses to target movement within a single hemifield [11]. Only two dragonfly TSDNs (DIT3 and MDT3) exhibit responses that extend more than 10° into the opposing hemifield, and the responses within only that opposing hemifield are not directionally tuned (Figure 2C) [11]. In contrast, the receptive fields of demoiselle TSDNs often extend beyond 20° across the visual midline and maintain the directional tuning across both hemifields (Figures 2C, 4, and S3C). Next, we investigated how such bilateral receptive fields arise in demoiselle damselflies.

### Demoiselle Damselfly TSDNs Are Binocular and Exhibit Binocular-Only, Ocular-Balanced, or Ocular-Dominant Responses

To investigate how the extension of receptive fields across the visual midline in demoiselle TSDNs relates to inputs from either eye, we recorded TSDN responses under monocular conditions where one eye was occluded with an opaque eye patch. Compared to the uncovered control conditions, all TSDNs exhibited a significant drop in spike numbers when either eye was covered (Friedman test for repeated measures with post hoc sign test; p = 0.00014; n = 12; Figures 5 and S5B), demonstrating that demoiselle TSDNs depend upon simultaneous binocular inputs. For all cells recorded, the hemifield ipsilateral to the patched eye had very low activity relative to controls (Figures 5A–5C; relative response integral <0.5; Figure S5B), which is consistent with the patch fully occluding visual input from that side. However, we saw varying responses in the hemifield that corresponded to the unoccluded eye, which we will refer to as the "contralateral hemifield" (as it is contralateral to the patch). We categorized these responses into three types.

In type 1 responses, the contralateral hemifield activity was low regardless of whether the patch was on the right or left (Figure S5A), indicating these responses belonged to neurons that were exclusively binocular with visual responses dependent on both eyes contributing in an all (binocular) or none (monocular) fashion (Figures 5A, n = 3 cells from 2 animals, and S5B). Very few spikes were observed in each monocular condition, and those present were mostly in the non-occluded visual hemifield, suggesting that the contralateral eye was not accidentally occluded (Figure 5A). This binocular-only group implies that, for these neurons, monocular responses to a moving target do not reach the threshold required to fire the TSDN but that such threshold is reached by the combination of both monocular responses at or upstream of the TSDN (Figure 5A, model).

Type 2 responses exhibited moderate, if variable, activity in the contralateral hemifield whether the patch was on the left or right eye (Figure S5; n = 4 cells from 4 animals). Hence, in TSDNs with type 2 responses (Figure 5B), the single unoccluded eye that was not patched sufficiently excited the neuron to fire. We speculate that the input weighting from each eye is balanced in these neurons and, by combining the two monocular responses, binocular contributions synergize to increase spike numbers
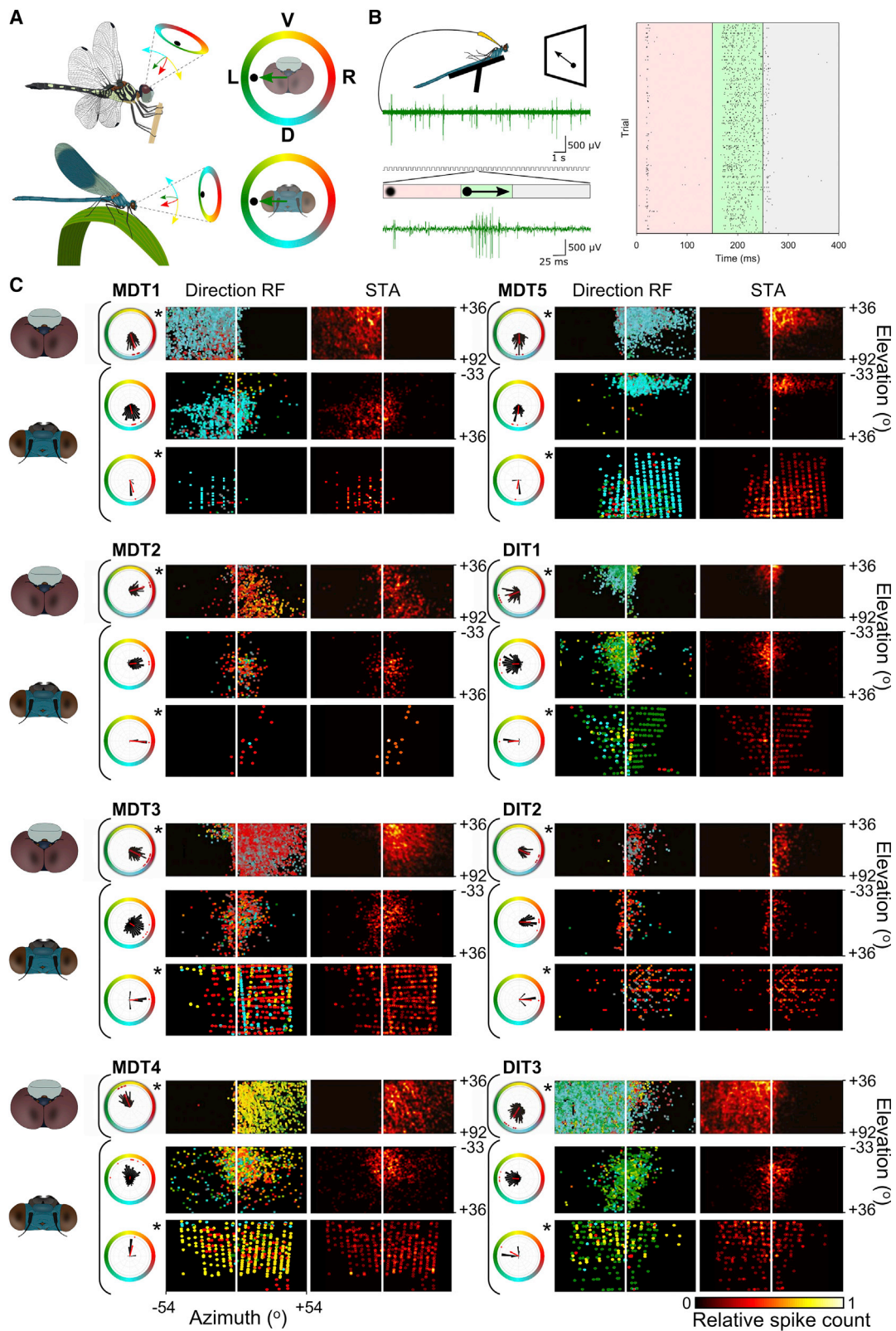
**Figure 2. Target-Selective Descending Neurons (TSDNs) in Damselflies**

(A) In damselflies, there is a ventral shift relative to dragonflies in the receptive field of target responses recorded from the ventral nerve cord (see Figure S2A). Apart from this elevation difference, the color wheel used to encode direction is equivalent in both animals in keeping with the coordinate system used in [11].

*(legend continued on next page)*

across the entire receptive field (Figure 5B, model). It is possible that the difference between type 1 and type 2 responses is due to different spiking thresholds (i.e., sensitivity) at the time of the experiment (Figure 5B, model), a TSDN property that we had previously observed in our intracellular recordings (Figure 4).

Type 3 responses were asymmetrical in that we observed contralateral hemifield activity when the patch was on the right, but not when the patch was on the left (Figure S5; n = 5 cells from 5 animals). Hence, the neurons in this category exhibit "left ocular dominance." This response pattern could arise from a similar summation-to-threshold mechanism as type 2 responses but with ocular weightings that are not balanced, and thus, only one visual hemifield can reach threshold under monocular conditions (Figure 5C, model). It is possible that the different threshold sensitivities and ocular weightings are in fact invariant properties of individual TSDNs types, but we cannot resolve whether this is the case from our extracellular data in this experiment, because some of the TSDN responses have directional tuning responses and receptive field locations similar to each other (but see Figure S5B for putative TSDN ID allocation for the recordings in this experiment).

### Differences in Global Light Level Do Not Underlie the Binocular Input Requirements of TSDNs

Our results above demonstrate that target tracking at the pre-motor stage in demoiselles depends on binocular input. Do TSDNs require that both eyes perceive a discrete moving target or is the observed dependence a result of a decrease in global luminance in the patched eye (see, for example [28])? To test this possibility, we compared monocular responses resulting from eyepatches made of either an opaque or translucent material (Figure 6A; n = 3 cells from 2 animals; cells 1 and 2 were recorded simultaneously from the same animal). Note that, for this experiment, a reduced mapping stimulus was used (also chosen for intracellular recordings). This resulted in sparser receptive field maps, with lines of activity arising from the longer, rasterized target trajectories presented across the visual field. This stimulus choice aimed to maximize the number of conditions per recording. The translucent eyepatch functioned to diffuse target contrast details within the visual field, such that no TSDN target responses were observed when both eyes were covered, although overall changes in light level still made the neuron fire, as seen in the preservation of wide-field ON-OFF responses (Figures S6A and S6B). All three types of binocular responses described above were observed again under both opaque and translucent monocular conditions, with no obvious differences

in spike firing rates between the two eyepatch materials (Figure 6A). This demonstrates that the abolition of demoiselle TSDN spike firing for type 1 responses and the reduction of spike firing in the contralateral uncovered visual hemifield of type 2 and 3 responses do not arise from global luminance intensity differences between both eyes. Instead, this lack of response appears to result from an unsatisfied requirement of demoiselle TSDNs for simultaneous stimulation of each eye by a moving target.

### Demoiselle TSDN Receptive Fields Resulting from Reduced Binocularity Are Consistent with Binocular Summation

Given that target-tracking responses from both eyes are necessary to drive demoiselle TSDNs effectively, we next investigated whether reducing the level of binocular overlap between the two eyes would result in similarly dramatic changes to the TSDN receptive fields. We speculated that a small decrease in binocular overlap (i.e., 4°) would not have a significant impact in the ability of the TSDN to summate to threshold over the majority of its response, and thus, spike numbers would be similar to control. In contrast, a large drop in binocular overlap (i.e., 10°) should result in the TSDN failing to reach threshold and thus lead to a lower number of spikes.

For this test, we placed wedge prisms in front of one or both eyes that deviated the visual scene by either 4° or 10° to the left of the animal. When placed over only the left eye, the prism decreases binocular overlap compared to uncovered controls (Figure S6C). As a control, we placed prisms over both eyes, shifting the entire visual field to the left. As expected, shifting global visual input also shifted the receptive field with the 4° prism (two-sided sign test for matched pairs; 4° deviation: p = 0.004; Figure 6B, blue densities). The receptive field also shifted under 10° prism, although it did not reach statistical significance (two-sided sign test for matched pairs; 10° deviation: p = 0.07; Figure 6B, blue densities). The receptive field densities continue to resemble Gaussian distributions when the prism covers both eyes. Subtracting the prism-both shifted density (B) from that of the uncovered condition (U) generates a curve antisymmetric about the vertical axis, resembling a sinusoid, as expected for two Gaussians of similar width and offset medians (Figure 6B, bottom row, B-U [prism both - uncovered]).

When we used a prism over the left eye to reduce binocular overlap by 4°, there was no significant reduction in spike density within the receptive field (two-sided sign test for matched pairs; p = 1.0; n = 9 cells from 6 animals; Figure 6B). This is in contrast

(B) Setup and stimulus presented when recording target responses extracellularly from a demoiselle ventral nerve cord. Visual stimuli are composed of 3,000 target trajectories with random motion direction and start location but fixed size and velocity, as used in dragonflies [11], allowing for comparative analysis. Top trace: raw responses to 44 trajectories indicated by steps on the stimulus trace (middle) are shown (scale, 1 s and 500 μV).. Bottom trace: responses to a single target trajectory where a target appears and remains stationary on the screen for 150 ms (red), moves with constant velocity (i.e., direction and speed) for 100 ms (green), and disappears for 150 ms (gray) before the start of the next trajectory are shown (scale, 25 ms and 500 μV). The raster plot shows a subset of responses used to map the cell's receptive field (time is measured from stimulus onset). Further details for the analysis workflow are shown in Figures S2C, S3A, and S3B. (C) Comparison between the receptive field maps of TSDNs in dragonflies and demoiselle TSDNs. All dragonfly maps were intracellularly acquired and are here reproduced from [11]. The damselfly recordings, both extracellular and intracellular, show one recording (for all extracellular recordings, see Figure S3C). The direction receptive field (RF) shows the position and direction of the target that elicited the spike. The spike-triggered average (STA) displays the relative spiking activity across the receptive field, normalized to maximum number of spikes in that recoding in any one screen location (pixel). Polar histograms represent the binned target direction for each spike (10° bins, black bars) and the resultant vector (red arrow) for the example receptive field. The red dots indicate the resultant vector direction for all neurons recorded. Elevation and azimuth scale are relative to the animal's head axis. The different types of TSDNs are labeled with their names (i.e., MDT1-5 and DIT1-3). The symbol * next to a map notes that it was acquired intracellularly.
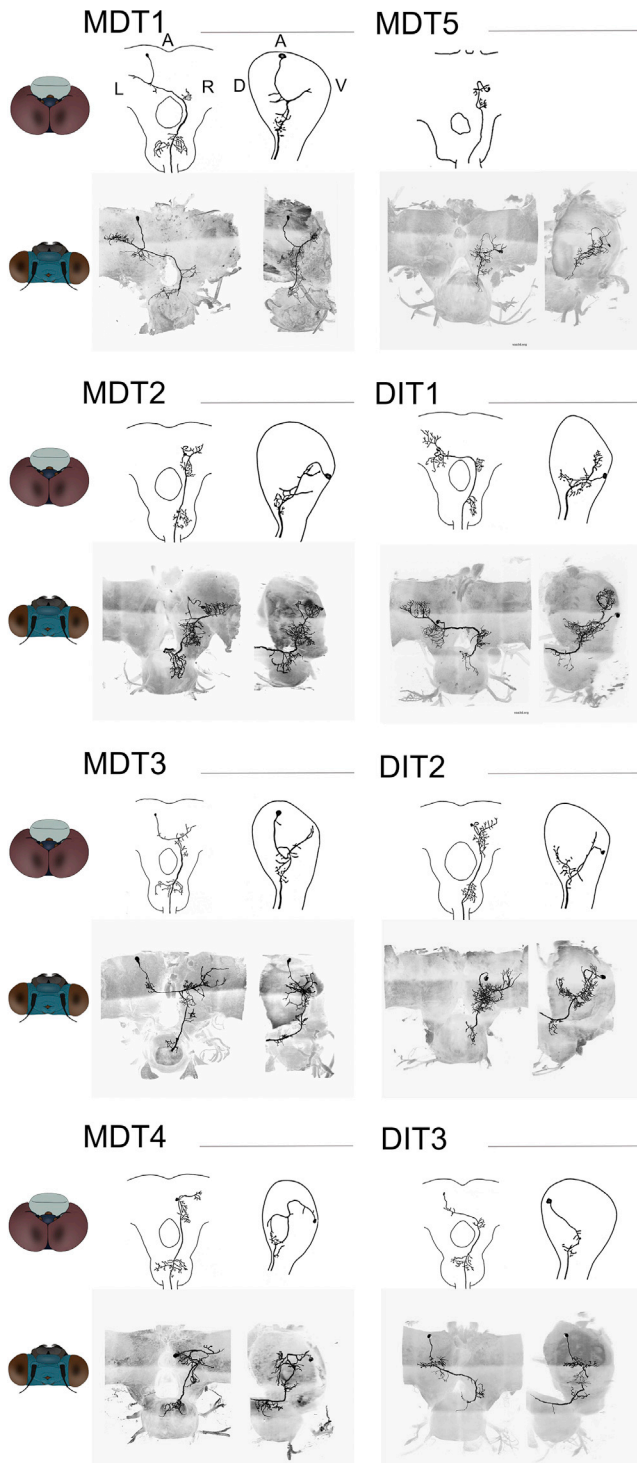
**Figure 3. The TSDNs in Damselflies and Dragonflies Are Homologous**
TSDN traces of the damselfly neurons whose intracellular maps are shown in Figure 2, shown in comparison with the traces of TSDNs in aeshnid dragonflies (reproduced with permission from [13, 20]). The raw maximum intensity projection data and the corresponding traces are shown for each cell in Video S3; the full 3D views are shown in Video S4. In addition, see Figure S4 for details about a possible new type of TSDN, found in damselflies.

to the attenuation observed in monocular occluding experiments (Figures 5 and 6A) and is consistent with summation of two monocular responses, with the offset monocular response (left eye) still sufficiently overlapping with the other (right eye) to reach threshold when combined. Indeed, under these 4° deviation conditions, the receptive field widens to the left (Figure 6B, ellipses), with a higher number of spikes seen in the entirety of the left hemifield (Figure 6B, bottom row, compare L-U [prism left - uncovered] and B-U, thin lines). This is as expected from monocular inputs that are moved further apart, albeit still overlapping in their areas of peak sensitivity. In contrast, when a more powerful prism reduced binocular overlap by 10°, the relative response within the receptive field was attenuated significantly (two-sided sign test for matched pairs; p = 0.0078; n = 8 cells from 7 animals; Figure 4B, compare purple densities and bottom row L-U). This indicates that, at this deviation power, the two monocular responses are sufficiently offset such that the summed TSDN response is no longer able to reach threshold, analogous to what was observed under monocular occluding conditions (Figures 5 and 6A).

## DISCUSSION

### Hunting Strategy, Eye Morphology, and TSDN Homology within Odonata

Damselflies and dragonflies share a last common ancestor ~270 mya and have thereafter evolved distinct behavioral and anatomical divergence, most notably in predatory tactic [9], flight kinematics [29], and ocular configuration [8, 9, 24]. Dichoptic eyes resembling those of Zygoptera and lower Epiprocta are present in fossils of extinct early odonates [8, 23], suggesting a dichoptic ancestral morphology among Odonata. Our behavioral data demonstrate, with regards to body orientation, the more frontal angle of attack in demoiselles compared to the dorsal path of libellulid dragonflies (Figures 1B, 1C, S1B, and S1C).

Although our high-speed videos do not have the resolution required to quantify the orientation of the head axis relative to the body axis, we know that an offset between these two axes exists in the dragonfly and demoiselle species here investigated. For example, when *Erythemis simplicicollis* is perched in our arena in preparation for hunting, we estimate that the head is tilted ventrally by ~30° with regards to the body axis (Figure S1D). Similarly, when ready for hunting, a demoiselle perches with its body axis pitched downward (~12°) and with its head pitched dorsally by the same amount (Figure S1E). Therefore, we estimate that, on average, *E. simplicicollis* responds to prey that is ~63° above the dragonfly head axis (Figure S1D). This is consistent with the high-acuity dorsal fovea of this species, which is positioned at 60° elevation [10], and within the preferred hunting range of 57°–102° in elevation previously reported for common white tail dragonflies (*P. lydia*) [15]. Likewise, we can estimate that, on average, a demoiselle responds when the prey is flying ~2° above its head axis (Figure S1E). This also fits well with the location of the visual fovea published for other damselfly species as directed forward and slightly downward [24, 30]. Given such estimations, we predict that the differences in the attack (i.e., dorsal-dragonfly and frontal-demoiselle) here reported between the two groups would be even more
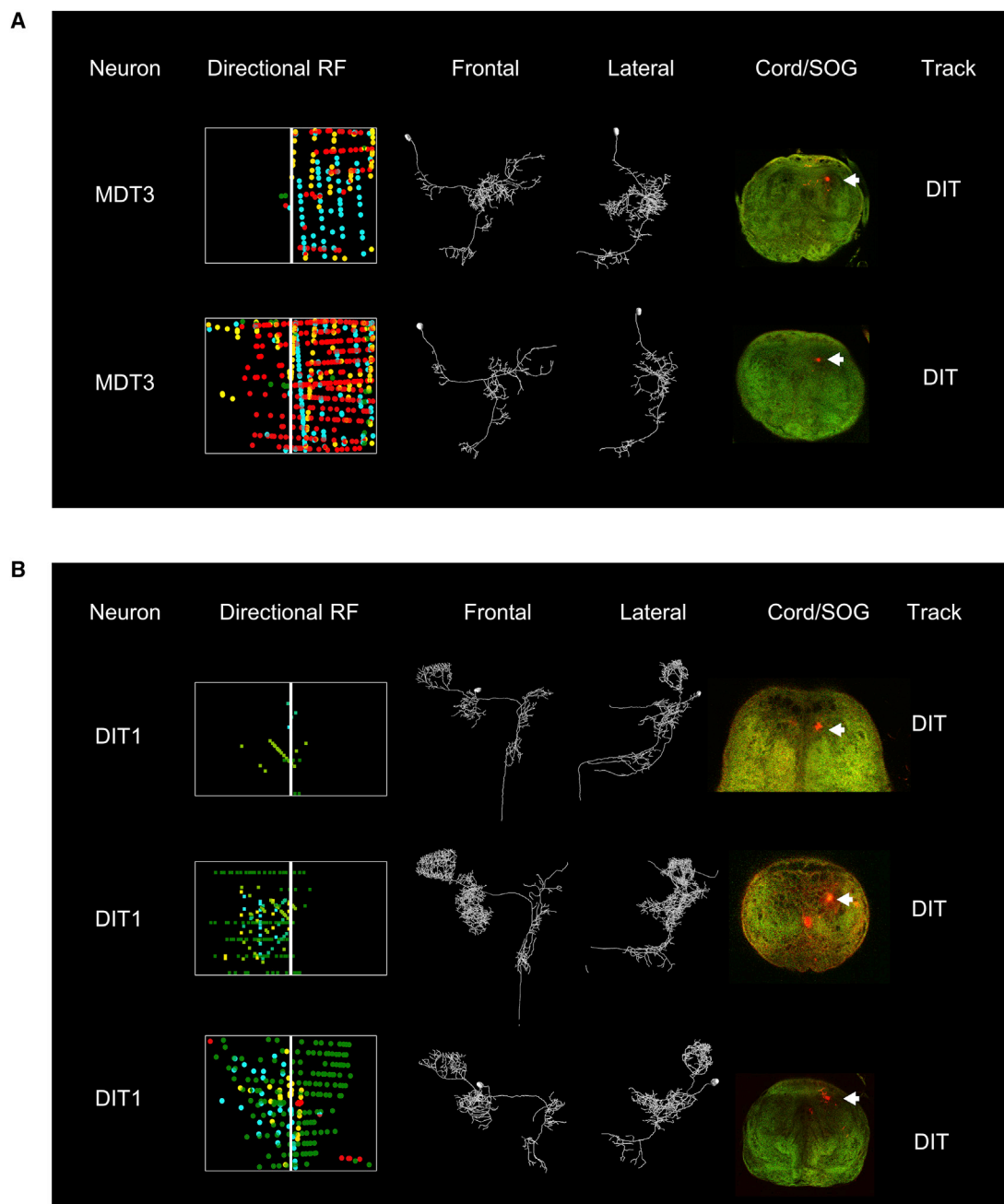
**Figure 4. Spike Number and Degree of Binocular Overlap within the Same Type of TSDNs Shows High Variability between Damselfly Individuals**

We used the directional tuning (from electrophysiology) and the neuronal morphology (from dye fills) to identify that we had recorded from (A) MDT3 and (B) DIT1 in two and three animals, respectively. The high variability in spike numbers and in the binocular overlap for each of these two TSDN types can be appreciated in such maps. Note that MDT3 was so named because it travels through the MDT track in Aeshnid dragonflies [13], but it travels though the DIT track in libellulids [11] and in demoiselles (this study).

pronounced if the measurements of the prey elevation were made relative to the head axis instead (i.e., prey location within the visual field of the predator).

Together, the behavior and the alignment of homologous TSDN receptive fields to the frontal and dorsal aspect of the visual field, respectively (Figures 2, 3, and S2), suggests that an ancestral target-tracking neuronal circuitry was inherited by these sister lineages and co-evolved with divergent ocular anatomy and predatory strategies.

Despite the distal ancestry between damselflies and dragonflies, TSDN receptive field architecture and anatomy are remarkably conserved (Figures 2 and 3). Demoiselle TSDNs
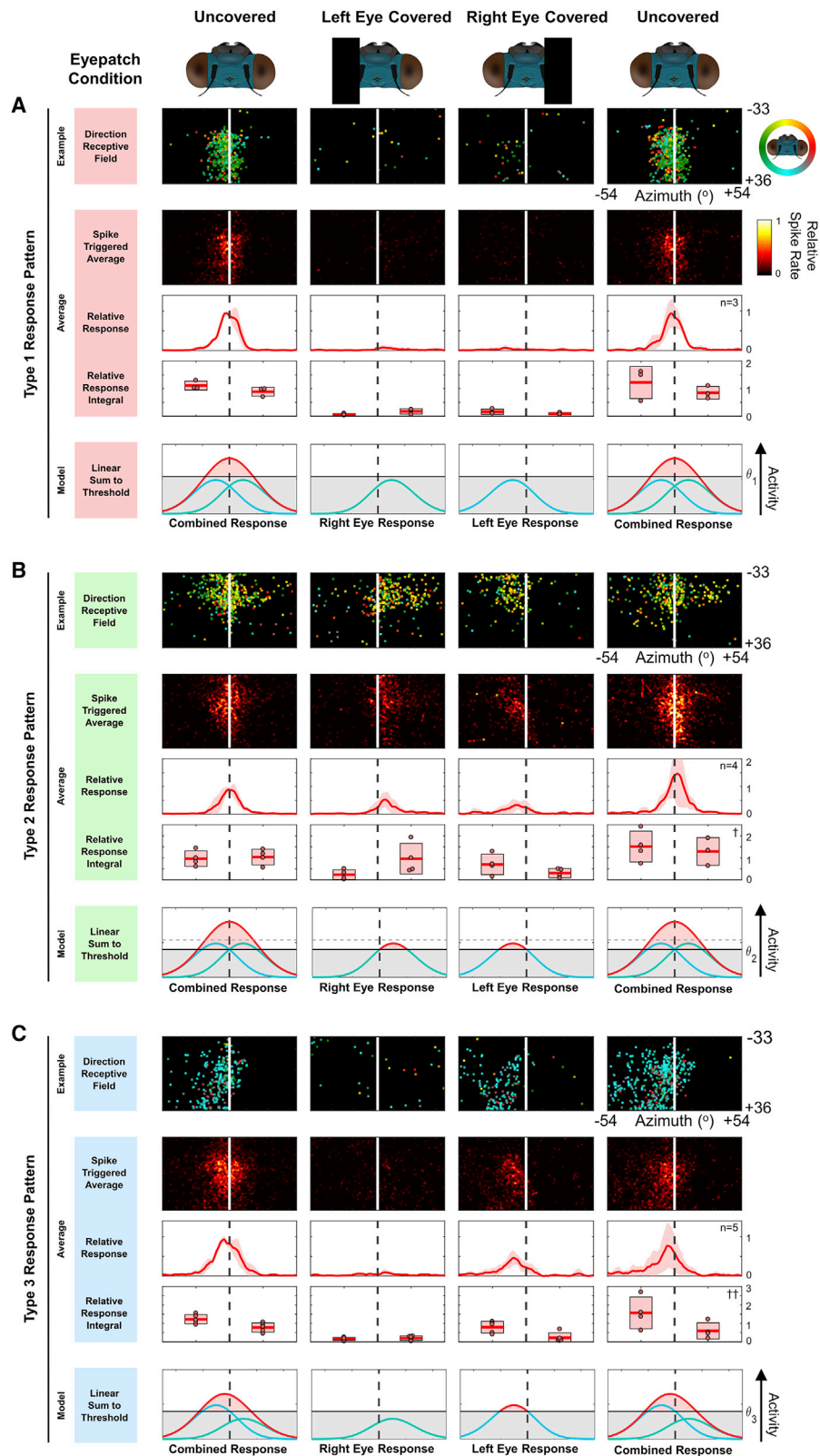
**Figure 5. Demoiselle TSDNs Are All Binocular, with Differing Thresholds and Input Weights**

TSDNs were mapped under binocular (equivalent to Figure 2) and monocular conditions (left and right eye patches, in random order), followed by another binocular map as a control. Monocular responses were categorized into three types (types 1–3, A–C, respectively), according to the binocular interaction

*(legend continued on next page)*

are directionally tuned, with some demoiselle TSDNs often indistinguishable from those in the dragonfly based on directional selectivity. This was somewhat surprising given the dissimilarity in flight kinematics in these sister lineages [29] and suggests that pre-motor encoding is robust to peripheral idiosyncrasies in flight actuation. It would be interesting to compare motor circuitry downstream of TSDNs in the thoracic motor centers to investigate whether peripheral circuitry is similarly robust to flight kinematics or whether these circuits are the subject of specialization [31].

### Neuronal Encoding of Holoptic versus Dichoptic Visual Space

Holoptic eyes have evolved independently in other insect lineages and, aside from dragonflies, are especially common among dipteran males who intercept or pursue fast flying females, including hoverflies, horseflies, and soldierflies [19]. Functionally, holoptic eyes are believed to aid in tracking small, fast-moving targets, although this is mechanistically poorly understood [19]. For example, holoptic eyes are usually associated with a dorsal bright or acute zone, where resolution is increased by flattening the ommatidial plane to reduce interommatidial angles [19, 32]; however, this advantage alone is attainable without dorsal fusion of the eyes, as is found in robber flies [33] and mantids [34].

Our comparative work suggests that, in Odonata, the reference frame within which a target is encoded differs between holoptic and dichoptic eyes. Because demoiselle TSDNs are directionally tuned, and because their responses are dependent on the summation of input from both eyes, they encode directional information in a binocular-fused frame of reference, i.e., information of a target moving toward the midline in the left eye must be combined with information of the target moving away from the midline in the right eye. This is in contrast to the TSDNs of holoptic *Aeshnoidea* and *Libellulidea* dragonflies, whose receptive fields possess a sharp midline boundary [11, 13, 20] and thus encode target motion with a frame of reference that is relative to their sagittal plane. It is possible that the sharpening of this midline boundary in dragonfly TSDNs has co-evolved with the holoptic eye and functions to simplify the pre-motor representation of the visual scene by encoding movement of targets in each eye as two halves of a visual panorama. This sagittal reference frame explicitly represents target movement with respect to the holoptic midline and thus aligns the sensory coordinate system to represent lateralized commands for the thoracic motor centers. This design may enhance the efficiency of neuronal processing for rapid and accurate responses in interception strategies that do not require stereoscopic information, as is thought to be the case in *Libellulidea* [15]. We would expect other holoptic species to employ a similarly lateralized simplification of pre-motor target movement representations.

### Binocular Properties of Demoiselle TSDNS

We have shown that the responses of demoiselle TSDNs to small moving targets are highly or entirely dependent on simultaneous binocular stimulation (Figures 5 and 6). In insects, binocular neurons that assess self-motion through wide-field optic flow includes those of the lobula complex [35–37], descending neurons [38, 39], and motor neurons [40]. Such binocular wide-field neurons respond strongly to monocular stimulation, and binocular integration functions to extend the receptive field across the visual panorama to enhance directional selectivity and match specific modes of self-motion [35, 37, 39, 40]. Further studies document binocular integration of moving objects in the lobula complex of crabs, mantids, and dragonflies [17, 41, 42]. The dragonfly centrifugal neuron (CSTMD1) responds to small moving objects with an extended receptive field across the two visual hemispheres and is thought to attend to targets moving from one visual hemisphere to the other [17]; in this respect, the function of binocular integration appears to be to extend the receptive field, similar to binocular optic flow neurons [35]. In crabs and mantids, lobula neurons typically respond to independent monocular stimulation with vertical bars, but simultaneous stimulation of both eyes changes (increases or decreases) those responses [41, 42]. In the case of mantids, binocular responses are consistent with a linear summation to threshold mechanism [42]. Thus, given that demoiselle TSDNs appear to sum monocular responses to threshold (Figure 5), it is possible that mantis and demoiselle object-tracking circuits may integrate binocular information similarly, earlier in the visual system.

Without anatomical verification for the eye patch experiments, we are currently unable to conclude whether the three types of binocularity patterns recorded in this study pertain to specific TSDN types, so this possibility remains to be investigated. However, we know that the extent of binocular overlap can change dramatically within a TSDN type across animals (Figure 4) and that simultaneously recorded TSDNs in the same animal exhibit different binocularity patterns (Figure 6A), evidencing that differences in binocularity are present within an individual and across the population. Our results suggest that such differences could arise from changes in eye dominance (weighing of inputs) and

---

observed. For each response type, row 1 is representative direction receptive field map from a single cell (example), row 2 is average spike-triggered map from cells falling within the category, row 3 is relative response densities (STAs projected onto the horizontal axis; mean ± SD for each cell recording), row 4 is left versus right hemifield relative response cumulative sum, and row 5 is proposed summation-to-threshold model that could generate the responses. Full data are given in Figure S5B. Direction map color-coordinated system indicated by the colorwheel. Spike triggered average maps are color-coded as relative spike rates between 0–1, as indicated by the scale bar.

(A) Type 1: binocular only, in which visual responses are dependent on both eyes in an all-or-none fashion. n = 3 cells allocated to this category.

(B) Type 2: balanced split-monocular, in which receptive fields are bisected along the midline with absent responses from the hemifield ipsilateral to the eyepatch and reduced responses, but still present, in the contralateral hemifield (arising from non-occluded eye). n = 4 cells allocated to this category. †For 1 cell, the right eye hemifield of this second control had an unusually high relative response. This hemifield was noted as an outlier, possibly caused by electrode or animal movement, and excluded from mean/variance calculation.

(C) Type 3: ocular dominant, in which occlusion of one eye fully suppresses the entire receptive field. However, occlusion of the adjacent eye bisects the receptive field at the midline with responses found only in the non-occluded hemifield. n = 5 cells allocated to this category. ††One type 3 cell is missing the uncovered positive control due to deterioration of recording signal (see Figure S5B).
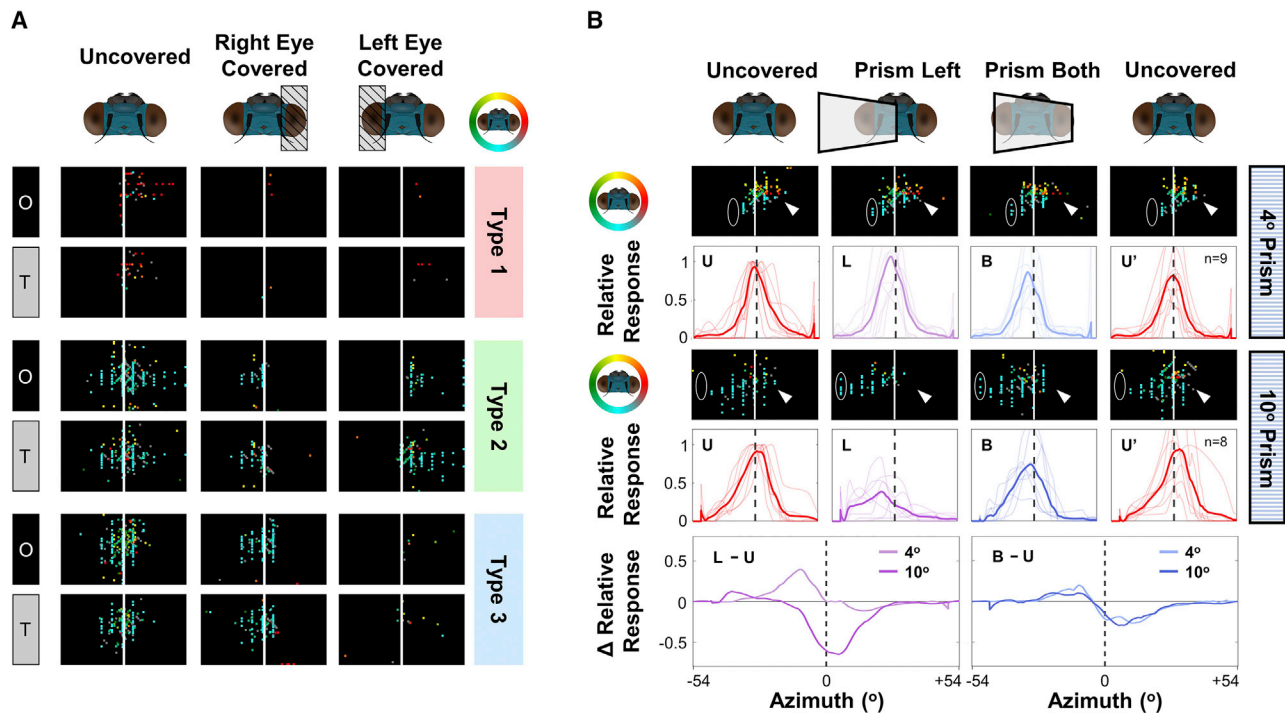
**Figure 6. Demoiselle TSDN Receptive Fields under Opaque versus Translucent Eyepatches and Prisms**

(A) The effect of global intensity on the TSDNs responses was tested by mapping them with opaque (as in Figure 2) and translucent eye patches (noted with letters O and T; see also Figures S6A and S6B). All three types of response categories described in Figure 2 were also found in this experiment. Receptive fields were recorded in series (i.e., binocular uncovered, left/right opaque eyepatch, binocular uncovered, left/right translucent eyepatch, and binocular uncovered—the final binocular uncovered condition is excluded for presentation clarity).

(B) A 4° and a 10° prism were used to test the TSDN responses under reduced binocular overlap between the two eyes (base out over left eye, producing deviation toward the left; Figure S6C). Reducing binocularity by 4° did not significantly affect spike density (two-sided sign test for matched pairs; p = 1.0; n = 9; blue traces), but a shift of 10° significantly lowered the spike densities compared to uncovered control (two-sided sign test for matched pairs; p = 0.0078; n = 8; see purple traces). No prism or prism over both eyes served as controls for the effect of the prism. Rows 1 and 3 show three example directional receptive fields at each prism deviation. White arrowheads mark the right-hand boundary of the receptive field. White ellipses indicate the left-hand boundary of the receptive field. Rows 2 and 4 are relative response densities (STAs projected onto the horizontal axis; mean ± individual traces from each recording; 4° n = 9 cells from 6 animals; 10° n = 8 cells from 7 animals). Row 5 shows Δ-relative response plots calculated by subtracting the first binocular uncovered response density (control) from each condition. B, binocular prism; L, monocular prism over left eye; U, uncovered; U', uncovered control. Full dataset for prism experiments is in Figure S6D.

sensitivity (threshold). Changes in eye dominance can result from experience-driven plasticity [43]. Because dragonfly TSDNs remain silent for the first 1 to 2 days after eclosion (R.M.O., unpublished data), input weightings may be fine-tuned during this period. With regards to differences in threshold sensitivity, it is known that the same TSDNs recorded in different individuals of the same dragonfly species exhibit markedly different spiking levels [11], a finding reproduced here in demoiselles (Figure 4). This is likely a combination of recent stimulus history (repeated stimulation quickly results in a reduction of responses due to habituation) and internal state (such as hunger, temperature, or maturity level). Indeed, in the stomatogastric system of crabs and lobsters, the properties of individual neurons forming a circuit vary across animals, but all populations reach an equilibrium that produces a common motor output [44, 45].

Although demoiselle TSDN receptive fields are binocular and receive bilateral input, our monocular (Figures 5–6A) and prism experiments (Figure 6B) indicate that the visual midline is nonetheless encoded within the inputs to these neurons. It is not clear from our data how a binocular TSDN threshold becomes positioned at the visual midline to yield the truncated type 2 and

type 3 monocular receptive fields (Figures 5–6B). It is possible that interocular inhibition may be at play to fine-tune the positioning of this threshold. Indeed, in the dragonfly lobula, heterolateral inhibitory feedback between centrifugal CSTMDs results in an abrupt decrease in firing rate as a target crosses the midline from the ipsilateral into the contralateral visual hemisphere [17, 46]. Analogous circuitry in the demoiselle lobula may function to define a visual midline that could feed into threshold tuning.

In summary, we have presented evidence that target tracking information at the pre-motor level is fused across visual hemispheres in demoiselles. Binocular fusion is known to confer perceptual advantages relevant for a target tracking system, such as enhanced visual sensitivity [2, 3] and decreased reaction times [4]. However, such binocular fusion necessitates encoding visual motion in a binocular-fused frame of reference. In contrast, the reference frame of holoptic eyes is relative to the midline. This may result in a simpler descending control system that only needs to implement the commands from one eye/neuron, preventing the temporal resolution problems that may arise when integrating equivalent signals from neurons with different sensitives and latencies. As a trade-off, the holoptic eye is limited

in stereoscopic computation of depth compared to a dichoptic morphology. Our data indicate that demoiselle TSDNs are disrupted when their binocular overlap is reduced by more than 10°. It remains to be shown whether these binocular neurons respond to disparities and whether a population of disparity-tuned cells, which could be used for stereoscopic processing of depth, is present earlier in the demoiselle visual system.

## STAR★METHODS

Detailed methods are provided in the online version of this paper and include the following:

- KEY RESOURCES TABLE
- LEAD CONTACT AND MATERIALS AVAILABILITY
- EXPERIMENTAL MODEL AND SUBJECT DETAILS
  - Animals
- METHOD DETAILS
  - High-speed Video Recordings of Predatory Behavior
  - Behavioral Analysis
  - Visual Stimuli
  - Extracellular Electrophysiology Recordings
  - Intracellular Electrophysiology Recordings
  - Whole Brain Imaging
- QUANTIFICATION AND STATISTICAL ANALYSIS
  - Electrophysiology Analysis
- DATA AND CODE AVAILABILITY

### SUPPLEMENTAL INFORMATION

Supplemental Information can be found online at https://doi.org/10.1016/j.cub.2019.12.031.

A video abstract is available at https://doi.org/10.1016/j.cub.2019.12.031#mmc7.

### AUTHOR CONTRIBUTIONS

J.A.S., C.K., T.J.W., and P.T.G.-B. designed the study. J.A.S., S.T.F., M.L., D.G., and S.P. collected behavioral data. J.A.S. and S.P. analyzed the behavioral data. J.A.S. and D.P.-B. carried out the extracellular experiments and analyzed the data. P.T.G.-B. and R.M.O. carried out the intracellular recordings, and R.M.O. and J.A.S. analyzed the data. J.A.S., T.J.W., and P.T.G.-B. processed and imaged the brain samples. H.P. and Y.W. developed tools for neuron reconstruction and profiling. H.P. and L.L. managed the generation of reconstructions of J.P. and S.J. and performed the proofreading. J.A.S. and P.T.G.-B. wrote the first draft.

### REFERENCES

1. Barendregt, M., Harvey, B.M., Rokers, B., and Dumoulin, S.O. (2015). Transformation from a retinal to a cyclopean representation in human visual cortex. Curr. Biol. *25*, 1982–1987.

2. Campbell, F.W., and Green, D.G. (1965). Monocular versus binocular visual acuity. Nature *208*, 191–192.

3. Elberger, A.J. (1989). Binocularity and single cell acuity are related in striate cortex of corpus callosum sectioned and normal cats. Exp. Brain Res. *77*, 213–216.

4. Blake, R., Martens, W., and Di Gianfilippo, A. (1980). Reaction time as a measure of binocular interaction in human vision. Invest. Ophthalmol. Vis. Sci. *19*, 930–941.

5. Ding, J., and Levi, D.M. (2011). Recovery of stereopsis through perceptual learning in human adults with abnormal binocular vision. Proc. Natl. Acad. Sci. USA *108*, E733–E741.

6. Nityananda, V., and Read, J.C.A. (2017). Stereopsis in animals: evolution, function and mechanisms. J. Exp. Biol. *220*, 2502–2512.

7. Lythgoe, J.N. (1979). Ecology of Vision (Oxford University Press).

8. Grimaldi, D.A., and Engel, M.S. (2005). Evolution of the Insects (Cambridge University Press).

9. Corbet, P.S. (1999). Dragonflies: Behaviour and Ecology of Odonata (Cornell University Press).

10. Olberg, R.M., Seaman, R.C., Coats, M.I., and Henry, A.F. (2007). Eye movements and target fixation during dragonfly prey-interception flights. J. Comp. Physiol. A Neuroethol. Sens. Neural Behav. Physiol. *193*, 685–693.

11. Gonzalez-Bellido, P.T., Peng, H., Yang, J., Georgopoulos, A.P., and Olberg, R.M. (2013). Eight pairs of descending visual neurons in the dragonfly give wing motor centers accurate population vector of prey direction. Proc. Natl. Acad. Sci. USA *110*, 696–701.

12. Mischiati, M., Lin, H.T., Herold, P., Imler, E., Olberg, R., and Leonardo, A. (2015). Internal models direct dragonfly interception steering. Nature *517*, 333–338.

13. Olberg, R.M. (1986). Identified target-selective visual interneurons descending from the dragonfly brain. J. Comp. Physiol. A *159*, 827–840.

14. Olberg, R.M. (1981). Parallel encoding of direction of wind, head, abdomen, and visual pattern movement by single interneurons in the dragonfly. J. Comp. Physiol. A *142*, 27–41.

15. Lin, H.T., and Leonardo, A. (2017). Heuristic rules underlying dragonfly prey selection and interception. Curr. Biol. *27*, 1124–1137.

16. O'Carroll, D. (1993). Feature-detecting neurons in dragonflies. Nature *362*, 541–543.

17. Wiederman, S.D., and O'Carroll, D.C. (2013). Selective attention in an insect visual neuron. Curr. Biol. *23*, 156–161.

18. Nordström, K., Bolzon, D.M., and O'Carroll, D.C. (2011). Spatial facilitation by a high-performance dragonfly target-detecting neuron. Biol. Lett. *7*, 588–592.

19. Perry, M.W., and Desplan, C. (2016). Love spots. Curr. Biol. *26*, R484–R485.

20. Frye, M.A., and Olberg, R. (1995). Visual receptive field properties of feature detecting neurons in the dragonfly. J. Comp. Physiol. A *177*, 569–576.

21. Olberg, R.C. (1978). Visual and multimodal interneurons in dragonflies. PhD thesis (University of Washington).

22. Nel, A., Prokop, J., Pecharová, M., Engel, M.S., and Garrouste, R. (2018). Palaeozoic giant dragonflies were hawker predators. Sci. Rep. *8*, 12141.

23. Bechly, G., Brauckmann, C., Zessin, W., and Gröning, E. (2001). New results concerning the morphology of the most ancient dragonflies (Insecta: Odonatoptera) from the Namurian of Hagen-Vorhalle (Germany). J. Zool. Syst. Evol. Res. *39*, 209–226.

24. Horridge, G.A. (1978). The separation of visual axes in apposition compound eyes. Philos. Trans. R. Soc. Lond. B Biol. Sci. *285*, 1–59.

25. von Reyn, C.R., Breads, P., Peek, M.Y., Zheng, G.Z., Williamson, W.R., Yee, A.L., Leonardo, A., and Card, G.M. (2014). A spike-timing mechanism for action selection. Nat. Neurosci. *17*, 962–970.

26. Rüppell, G. (1999). Prey capture flight of Calopteryx haemorrhoidalis (Vander Linden) (Zygoptera: Calopterygidae). Int. J. Odonatol. *2*, 123–131.

27. Ito, K., Shinomiya, K., Ito, M., Armstrong, J.D., Boyan, G., Hartenstein, V., Harzsch, S., Heisenberg, M., Homberg, U., Jenett, A., et al.; Insect Brain Name Working Group (2014). A systematic nomenclature for the insect brain. Neuron *81*, 755–765.

28. Zhou, J., Clavagnier, S., and Hess, R.F. (2013). Short-term monocular deprivation strengthens the patched eye's contribution to binocular combination. J. Vis. *13*, 12.

29. Wakeling, J., and Ellington, C. (1997). Dragonfly flight. II. Velocities, accelerations and kinematics of flapping flight. J. Exp. Biol. *200*, 557–582.

30. Walguarnery, J.W., Butler, M.A., and Schroeder, R. (2009). Visual Target Detection in Damselflies (University of Hawaii, Honolulu Department of Zoology).

31. Bidaye, S.S., Bockemühl, T., and Büschges, A. (2018). Six-legged walking in insects: how CPGs, peripheral feedback, and descending signals generate coordinated and adaptive motor rhythms. J. Neurophysiol. *119*, 459–475.

32. Labhart, T., and Nilsson, D.E. (1995). The dorsal eye of the dragonfly Sympetrum: specializations for prey detection against the blue sky. J. Comp. Physiol. A *176*, 437–453.

33. Wardill, T.J., Fabian, S.T., Pettigrew, A.C., Stavenga, D.G., Nordström, K., and Gonzalez-Bellido, P.T. (2017). A novel interception strategy in a miniature robber fly with extreme visual acuity. Curr. Biol. *27*, 854–859.

34. Barrós-Pita, J.C., and Maldonado, H. (1970). A fovea in the praying mantis eye. Z. Vgl. Physiol. *67*, 79–92.

35. Krapp, H.G., Hengstenberg, R., and Egelhaaf, M. (2001). Binocular contributions to optic flow processing in the fly visual system. J. Neurophysiol. *85*, 724–734.

36. Hennig, P., Kern, R., and Egelhaaf, M. (2011). Binocular integration of visual information: a model study on naturalistic optic flow processing. Front. Neural Circuits *5*, 4.

37. Farrow, K., Haag, J., and Borst, A. (2006). Nonlinear, binocular interactions underlying flow field selectivity of a motion-sensitive neuron. Nat. Neurosci. *9*, 1312–1320.

38. Wertz, A., Borst, A., and Haag, J. (2008). Nonlinear integration of binocular optic flow by DNOVS2, a descending neuron of the fly. J. Neurosci. *28*, 3131–3140.

39. Wertz, A., Haag, J., and Borst, A. (2009). Local and global motion preferences in descending neurons of the fly. J. Comp. Physiol. A Neuroethol. Sens. Neural Behav. Physiol. *195*, 1107–1120.

40. Huston, S.J., and Krapp, H.G. (2008). Visuomotor transformation in the fly gaze stabilization system. PLoS Biol. *6*, e173.

41. Scarano, F., Sztarker, J., Medan, V., Berón de Astrada, M., and Tomsic, D. (2018). Binocular neuronal processing of object motion in an arthropod. J. Neurosci. *38*, 6933–6948.

42. Rosner, R., von Hadeln, J., Tarawneh, G., and Read, J.C.A. (2019). A neuronal correlate of insect stereopsis. Nat. Commun. *10*, 2845.

43. Klink, P.C., Brascamp, J.W., Blake, R., and van Wezel, R.J.A. (2010). Experience-driven plasticity in binocular vision. Curr. Biol. *20*, 1464–1469.

44. Marder, E., and Goaillard, J.M. (2006). Variability, compensation and homeostasis in neuron and network function. Nat. Rev. Neurosci. *7*, 563–574.

45. Golowasch, J., Casey, M., Abbott, L.F., and Marder, E. (1999). Network stability from activity-dependent regulation of neuronal conductances. Neural Comput. *11*, 1079–1096.

46. Geurten, B.R.H., Nordström, K., Sprayberry, J.D.H., Bolzon, D.M., and O'Carroll, D.C. (2007). Neural mechanisms underlying target detection in a dragonfly centrifugal neuron. J. Exp. Biol. *210*, 3277–3284.

47. Wardill, T.J., Knowles, K., Barlow, L., Tapia, G., Nordström, K., Olberg, R.M., and Gonzalez-Bellido, P.T. (2015). The killer fly hunger games: target size and speed predict decision to pursuit. Brain Behav. Evol. *86*, 28–37.

48. Gengs, C., Leung, H.T., Skingsley, D.R., Iovchev, M.I., Yin, Z., Semenov, E.P., Burg, M.G., Hardie, R.C., and Pak, W.L. (2002). The target of Drosophila photoreceptor synaptic transmission is a histamine-gated chloride channel encoded by ort (hclA). J. Biol. Chem. *277*, 42113–42120.

49. Gonzalez-Bellido, P.T., and Wardill, T.J. (2012). Labeling and confocal imaging of neurons in thick invertebrate tissue samples. Cold Spring Harb. Protoc. *2012*, 969–983.

50. Preibisch, S., Saalfeld, S., and Tomancak, P. (2009). Globally optimal stitching of tiled 3D microscopic image acquisitions. Bioinformatics *25*, 1463–1465.

51. Schindelin, J., Arganda-Carreras, I., Frise, E., Kaynig, V., Longair, M., Pietzsch, T., Preibisch, S., Rueden, C., Saalfeld, S., Schmid, B., et al. (2012). Fiji: an open-source platform for biological-image analysis. Nat. Methods *9*, 676–682.

52. Peng, H., Bria, A., Zhou, Z., Iannello, G., and Long, F. (2014). Extensible visualization and analysis for multidimensional images using Vaa3D. Nat. Protoc. *9*, 193–208.

53. Bria, A., Iannello, G., Onofri, L., and Peng, H. (2016). TeraFly: real-time three-dimensional visualization and annotation of terabytes of multidimensional volumetric images. Nat. Methods *13*, 192–194.

54. Wang, Y., Li, Q., Liu, L., Zhou, Z., Ruan, Z., Kong, L., Li, Y., Wang, Y., Zhong, N., Chai, R., et al. (2019). TeraVR empowers precise reconstruction of complete 3-D neuronal morphology in the whole brain. Nat. Commun. *10*, 3474.

# STAR★METHODS

## KEY RESOURCES TABLE

| REAGENT or RESOURCE | SOURCE | IDENTIFIER |
|---|---|---|
| **Software** | | |
| MATLAB 2018, 2014, 2012, 2009 | The Mathworks | MATLAB, RRID:SCR_001622 |
| Python Programming Language | Python Software Foundation | RRID: SCR_008394 |
| SciPy | http://SciPy.org | RRID: SCR_008058 |
| StimulateOpenGL Version 20160216 | Janelia Research Campus | StimulateOpenGL_II |
| FIJI | NIH | Fiji, RRID:SCR_002285 |
| Vaa3D | HHMI, Allen Institute, and BrainTell (SEU-ALLEN) | Vaa3D, RRID:SCR_002609 |
| TeraVR | BrainTell (SEU-ALLEN) | https://github.com/Vaa3D/release/releases/ |
| TeraFly | BrainTell (SEU-ALLEN) | https://github.com/abria/TeraStitcher/wiki/TeraFly |
| Spike2 version 8 | Cambridge Electronic Design | Spike2 Software, RRID:SCR_000903 |
| Photron FASTCAM Viewer 3 Software (PFV3) | Photron | https://photron.com/software-downloads/ |
| **High Speed Videography Hardware** | | |
| Photron SA2 cameras | Photron | https://photron.com/fastcam-sa2/ |
| Photron Mini AX200 cameras | Photron | https://photron.com/mini-ax/ |
| 24 mm AF-S NIKKOR f/1.8G ED Nikon lenses | Nikkon | https://www.nikonusa.com/en/nikon-products/product/camera-lenses/af-s-nikkor-24mm-f%252f1.8g-ed.html |
| 85mm f/1.8D lens Nikon lenses | | https://www.nikonusa.com/en/nikon-products/product-archive/camera-lenses/af-nikkor-85mm-f%252f1.8d.html |
| **Electrophysiology Hardware** | | |
| NPI BA-03x amplifier | NPI Electronic | http://www.npielectronic.de/products/amplifiers/ba-bridge-amplifier/ba-03x.html |
| Humbug | Digitimer | https://digitimer.com/products/research-electrophysiology/hum-bug-noise-eliminator/hum-bug-ne/ |
| Micro1401-3 DAQ | Cambridge Electronic Design | http://ced.co.uk/products/micro3 |
| Tungsten Electrodes | Microelectrodes ltd. | https://www.microelectrodes.net,Tungsten 11-15 $\mu$m tip, 2-4MOhm impedance |
| **Eyepatches and Prisms** | | |
| Electrical insulation film | RS Components Ltd | Cat# 536-3980 |
| Wedge Prism 25RB12-01UF.AR2 | Newport | https://www.newport.com/p/25RB12-01UF.AR2, Cat# 25RB12-01UF.AR2 |
| 10-degree Press-On-Prism (20 diopter) | 3M | https://www.3m.com/3M/en_US/company-us/all-3m-products/~/3M-90-12000-PRESS-ON-Prism-20-00-Diopter/?N=5002385=3292952687&rt=rud, Cat# 90-12000) |
| **2-Photon Microscopy** | | |
| *In Vivo* Ultima Multiphoton Microscope | Bruker | https://www.bruker.com/products/fluorescence-microscopes/ultima-multiphoton-microscopy.html |
| Spectra-Physics InSight® DS+ laser | Newport | https://www.spectra-physics.com/products/ultrafast-lasers/insight-x3 |
| Olympus XLSL Plan N 25x /1.00 Glyc MP ∞/0-0.23/FN18 Multiphoton Objective | Olympus | https://www.olympus-lifescience.com/en/objectives/multiphoton Cat# XLSLPLN25XGMP |

*Continued*

| REAGENT or RESOURCE | SOURCE | IDENTIFIER |
| --- | --- | --- |
| Intracellular electrophysiology, dye loading and processing of dye filled brains | | |
| Fixable Lucifer Yellow Dye | Invitrogen | https://www.thermofisher.com/order/catalog/product/L1177 Cat# L1177 |
| Laser electrode puller | Sutter | Cat# P2000 |
| Glass electrodes | World Precision Instruments | Cat# TW100F – 4, OD of 1 mm and ID of 0.75 mm, Heat 340; Fil 4; Vel 50; Del 210; Pul 150. |
| Anti-Lucifer Yellow antibody conjugated with biotin | Thermo Scientific | Thermo Fisher Scientific Cat# A-5751, RRID:AB_2536191 |
| NeutrAvidin conjugated to DyLight 633, | Thermo Scientific | Cat# 22844, https://www.thermofisher.com/antibody/product/NeutrAvidin-Protein/22844 |
| Collagenase/dispase | Sigma-Aldrich | Cat# 10269638001, https://www.sigmaaldrich.com/catalog/product/roche/colldispro?lang=en&region=US |
| Hyaluronidase | Sigma-Aldrich | Cat# H4272, https://www.sigmaaldrich.com/catalog/product/sigma/h4272?lang=en&region=US |
| Universal antibody dilution buffer | Electron Microscopy Sciences | Cat# 25885, https://www.emsdiasum.com/microscopy/technical/datasheet/25885.aspx |
| TDE | Sigma-Aldrich | 99% 2,2'-Thiodiethanol, Cat# 166782, https://www.sigmaaldrich.com/catalog/product/aldrich/166782?lang=en&region=US |

## LEAD CONTACT AND MATERIALS AVAILABILITY

The lead contact for this article is Paloma Gonzalez-Bellido, paloma@umn.edu. This study did not generate new unique reagents.

## EXPERIMENTAL MODEL AND SUBJECT DETAILS

### Animals

Adult *Calopteryx splendens* were caught wild along the River Cam in Grantchester Meadows, Cambridge (UK), between May and August of years 2016-2018. *Calopteryx maculata* demoiselles were collected in York County, Pennsylvania (USA), during July 2017 and July 2019 with collection permission from park rangers. Between capture and experimentation, demoiselles were stored in humidified Petri dishes to avoid desiccation. Animals were typically used for experiments on the day of capture; however, animals stored for longer periods were refrigerated to improve longevity and were used within 4-5 days maximum. *Erythemis simplicicollis* dragonflies were reared from nymphs (Carolina Biological Supply Company) in the lab, with adults maintained in an indoor flight arena feeding on *Drosophila melanogaster*.

## METHOD DETAILS

### High-speed Video Recordings of Predatory Behavior

Two synchronized Photron SA2 cameras were used to film *Calopteryx maculata* demoiselles attacking artificial prey made from a silver 3 mm bead dangling on fishing line. The recordings were done either within a temporary outdoor plastic tent (York College) or unenclosed by a creek at Nixon State Park. *Erythemis simplicicollis* dragonflies hunting a black 3 mm bead were filmed using a similar dual synchronized Photron Mini AX200 camera system within an internal laboratory flight arena. High-speed recordings were carried out at 1000 frames per second with either a 24 mm AF-S NIKKOR f/1.8G ED Nikon lens or a Nikon 85mm f/1.8D lens.

### Behavioral Analysis

The dual image sequences from the synchronized camera systems were analyzed offline in MATLAB as previously described [33, 47]. Briefly, the two-camera system was calibrated for 3D reconstruction based on a checkerboard calibration sequence using scripts originally written in J.Y. Bouguet's laboratory (Caltech, http://www.vision.caltech.edu/bouguetj/calib_doc/). For each video, the two synchronized image sequences were digitized in MATLAB to yield two (x,y)-coordinate time series for three points of interest: 1. position of the prey (bead), 2. the predator's head, and 3. the posterior tip of the predator's abdomen. These three stereo (x,y)-coordinate times-series pairs were then reconstructed into 3D cartesian space using the checkerboard calibration [33, 47,].

   To trace the path of the prey relative to the predator's body axis during predatory flight, the body axis of the predator (digitised points 2 and 3, described above) from each frame of the recording were superimposed. Alignment assumed that the body axis

did not rotate around the roll axis during flight (an assumption representative of Odonate flight, see Videos S1 and S2). Prey positions were reported relative to the aligned body axis, with positive angles representing dorsal elevations above the body azimuth.

The average elevation of the prey just prior to the flight initiation was calculated as follows: the frame prior to the predator's first movement was identified for each flight, the elevation values were measured (from the 3D flight reconstruction at each frame), and a circular mean from all flights was then calculated. The confidence interval for this measure is shown as the shaded cones in Figure 1C. To estimate the elevation of the prey relative to the head axis before take-off (estimation used in the Discussion), the tilt angle between the body axis and the head axis was measured from macrophotographs (Figures S1D and S1E). The value of this offset was then applied to the elevation of the prey from body axis just prior to any movement of the predator.

The reported average and confidence intervals for the elevation of the prey, relative to the predator's body axis throughout flight, was calculated as follows: i. for each flight, an average elevation angle was calculated (i.e., circular mean of the values throughout a single trajectory) then, ii. the values obtained in (i) for each trajectory were averaged (i.e., circular mean of all the flights). The average trajectories shown as blue traces in Figure 1C were calculated as follows: i. normalizing each trajectory to the maximum distance between the predator and prey throughout flight, ii. binning along 5% radial intervals (0% predator's head, 100% maximum distance of the prey), iii. averaging the elevation and azimuth values within each bin for each individual flight (circular mean within a bin), iv. averaging each bin across all flights (circular mean of bins across flights). Statistical tests reported in the main text were performed using the Watson-Williams test for equality of means.

### Visual Stimuli

Visual stimuli were projected onto a 17.3 × 9.6 cm white screen using a DepthQ 360 projector (Cambridge Research Systems) with a spatial resolution of 1280 × 720 pixels running at 360 Hz, using StimulateOpenGL software (version 20160216, Janelia Research Campus, https://github.com/cculianu/StimulateOpenGL_II). Demoiselles were positioned 7 cm from the screen, giving a subtended projected screen size of 102 × 70 degrees. For initial receptive field mapping and monocular experiments, stimuli were chosen to match those described previously for comparison to Dragonflies [11]. This stimulus consisted of a sequence of 3000 target trajectories, with each trajectory composed of three phases (Figure S2): (1) a small (2x2 degree) target appearing stationary at a random position on the screen for 150 ms before, (2) moving in a random direction for 100 ms at constant speed (160 deg/s), followed by (3) a 150 ms delay before the next trajectory was presented. This method allows receptive fields to be mapped with high spatial resolution while avoiding fast habituation of the cell responses [11].

A different mapping technique, with a lower number of trajectories, was designed to allow the opaque versus translucent versus prisms comparison of TSDN responses. In these experiments, the target stimulus scanned across the screen with longer trajectories, covering only eight directions (up/down/left/right and diagonals). Target size and velocity was matched to the 3000 trajectory scans used in initial experiments (2x2 degree targets, 160 deg/s velocity). Translucent eyepatches were made using electrical insulation film which strongly diffuses the light but are thin enough so as not to drastically reduce luminance (RS Components Ltd, product 536-3980; Figure S4). A 4° deviation (Newport, 25RB12-01UF.AR2) or 10° deviation Press-On-Prism (3M, 20 diopter. Cat# 90-12000) was positioned horizontally with the thinnest edge of the wedge positioned medial relative to the eye to avoid occluding the contralateral eye. This prism orientation results in a lateral shift of the visual field relative to the eye in monocular experiments.

### Extracellular Electrophysiology Recordings

At experimental time, the animal was anaesthetised on ice, immobilized dorsal side down, and a small hole cut at the anterio-ventral thoracic surface to expose the ventral nerve cord. Extracellular recordings were performed as described previously (Nicholas et al., 2018). A sharp glass-insulated tungsten electrode (2-4 MOhm, Microelectrodes Ltd., Cambridge, UK) was inserted into the cervical connective, with mechanical support given to the cord by a small hook fashioned from a hypodermic needle. The animal was grounded using a saline-filled glass microelectrode inserted into the ventral cavity, which also served as the reference electrode (Fly saline as described in [48]: 138 mM NaCl, 2 mM KCl, 1.8 mM $CaCl_2$, 4 mM $MgCl_2$, 5 mM TES, pH 7.15). Hydration of the ventral cavity was maintained by continual capillary action from an additional saline-filled glass microelectrode. Extracellular signals were amplified at 500x gain and filtered through a 300 – 3000 Hz analog bandpass filter on an NPI BA-03x amplifier (NPI Electronic), filtered through a HumBug (Digitimer), digitized on a micro1401-3 DAQ (CED), and acquired at 25kHz with Spike2 software (CED). Measurements were taken at 23°C. Typically 1, but sometimes up to 3 units were recorded, and typically between 0 to 2 were TSDN responses. TSDNs have, by far, the largest axons of the cord. Therefore, they have the largest probability of being picked up by the electrode.

### Intracellular Electrophysiology Recordings

For intracellular recordings, the animals were prepared as described above for extracellular recordings. A metal spoon, made from a bent and polished needle, was then inserted into the cavity to 'hug' the cord and provide support. Glass electrodes (thin wall borosilicate glass with an OD of 1 mm and ID of 0.75 mm; WPI Cat# TW100F – 4) were pulled with a laser electrode puller (Sutter P-2000), by choosing the following settings: Heat 340; Fil 4; Vel 50; Del 210; Pul 150. Once the electrodes were filled with 1.5 or 3% Lucifer Yellow in 1M LiCl, or with 1M KCL, the resulting resistance was circa 80 or 20 MΩ, respectively. Negative current (total between −2 and −15 nA, depending on the preparation) was injected with square pulses (6 s on-1 s of), for as long as the cell was held, which was sometimes up to 1 hour. Measurements were taken at 23°C. In total, 17 TSDN cells were recorded intracellularly and filled (experiments were carried out in 17 different animals).

### Whole Brain Imaging

After dye filling the neurons, the animal was transferred to 4% paraformaldehyde overnight at room temperature. The day after, the preparation was washed with PBS, and the brain removed. The brain was then cleared following previous protocols [49]. Cleared brains were positioned into a small groove of Sylgard (Sigma-Aldrich) submerged in 97% TDE (2,2′-thiodiethanol). Brains were imaged using an Olympus XLSL Plan N 25x /1.00 Glyc MP ∞/0-0.23/FN18 multiphoton objective, a Newport Spectra-Physics In-Sight® DS+ laser at 920 nm, and a Bruker (Prairie Technologies) *in vivo* multiphoton microscope using GFP and RFP detection channels. Images were acquired as a tiled Z stack at 0.9 μm isovoxel resolution (Prairie View v5.4), and stitched in Fiji [50, 51]. Image stacks were converted into the TeraFly-compatible hierarchical representation and loaded into Vaa3D (http://vaa3d.org), with which the filled neurons were then traced [52–54]. For image regions with low signal-to-noise ratio (SNR) or containing complicated arborizations, TeraVR was adopted to achieve unambiguous tracing results [54]. Each neuron reconstruction was produced by two annotators collaboratively for tracing and proofing using TeraVR and TeraFly tools, based on a standardized data production protocol developed by SEU-ALLEN Joint Center for the whole-mouse-brain full-neuron-morphology project (unpublished data).

## QUANTIFICATION AND STATISTICAL ANALYSIS

### Electrophysiology Analysis

Extracellular spike sorting was performed in Spike2 software (Cambridge Electronic Design Ltd, UK) using principal component analysis on waveform shapes followed by manual clustering. i.e., after the experiment was finished, the clusters of spikes in PCA space were manually circled and designated as a unit (Figure S2C). This was done with tools built in Spike2 software, for this purpose. Because the spike shape often changes gradually over time during the recording, the spike template could fit these gradual changes, and thus allocate the spikes as responses from the same neuron. However, if there was an abrupt change in spike shape, this was normally due to a sudden change in the location of the electrode (i.e., maybe due to animal movement), and thus, the spikes were not classified as belonging to the same unit. An acceptable clustering to the experimenter, looked like a cluster that was separated from all other spikes. This is a qualitative judgement in the spike sorting procedure and is not quantified in this study (see Figure S2C). Intracellular action potentials were detected with a manual threshold, with no further classification required. All further analysis was performed in MATLAB (Mathworks). For receptive field mapping in Figures 2 and 3, we calculated the latency for each cell. This latency (i.e., the time between stimulus presentation and the time at which the resulting spike was recorded in the connective), was used to identify the location and direction of the target that caused the spike (Figure S3A). Adjusting spike times by subtracting this latency gives a more accurate timestamp to correlate exactly where the target stimulus was in the visual field when the response was initiated [11]. Direction field maps, direction histograms, and spike-triggered average (STA) maps were calculated as previously described [11]. For eyepatch and prism experiments, raw STA maps were summed along the elevation axis yielding raw azimuth STA densities. Raw azimuth densities were smoothed and normalized to the maximum density value in the first uncovered condition. Relative response integrals were calculated as the sum of the normalized azimuth densities in each visual hemisphere. All spike count data is given as mean ± std. Δ relative response plots were calculated by subtracting the normalized relative response density of the first binocular (uncovered) control from that of all other conditions.

## DATA AND CODE AVAILABILITY

All data generated was analyzed during this study. All analyses are found within this published article. Raw data supporting the current study have not been deposited in a public repository because it is too large but are available from the corresponding author on request.